GDCh Research Article Angewandte International Edition Chemie www.angewandte.org

How to cite: *Angew. Chem. Int. Ed.* **2025**, e202509504
doi.org/10.1002/anie.202509504

Fluorescence Probe **Hot Paper**

Localized Hydrolysis-Based Proximity Reporting Platform for Protein Hierarchical Structure Profiling

Wei Li, Yiran Li, Nan Wang, Hongyan Tian, Yadong Xue, Haiqi Wang, Shaoli Jiang, Songtao Cheng, Nan Feng, Ru Jia, Chao Yan, Xiaojian Wang, Lin Ding, and Huangxian Ju*

Abstract: The substrate-specific bond cleavage capability of hydrolases provides a unique strategy for engineering off-on switches. This prompted our hypothesis that confining hydrolases and substrates to distinct biomolecular hierarchies (e.g., a protein and its modifying glycans) could enable transmission of spatial proximity information through localized hydrolysis. Using New Delhi metallo-β-lactamase 1 (NDM-1), we developed a localized hydrolysis-based proximity reporting (LHPR) platform for in situ elucidation of the hierarchical architecture of glycoproteins. We constructed protein probes by conjugating target-recognizing molecules with NDM-1, and designed click chemistry-reactive, substrate-caged fluorescent molecules as glycan probes. Programmed NDM-1 activity enabled in situ protein-specific imaging of glycans via proximity-dependent activation within various biological specimens. Within a unified enzymatic framework, we successfully quantified distinct glycans of individual proteins and established the principle of protein-specific glycosylation stoichiometry analysis. Our work provides a powerful tool for developing glycoprotein-based disease biomarkers, therapeutic targets, and diagnostic approaches, offering new possibilities for precision medicine research.

Introduction

Enzymes are a class of biomolecules with efficient catalytic activity, among which hydrolases have single-substrate specificity. By caging functional molecules with hydrolase substrates, signal switch and functional activation can be modulated through hydrolysis reactions.[1–7] This mechanism has been widely used to study protein dynamics and functions,[8] establish early disease diagnosis approaches,[9] control therapeutic probe functions,[5] and guide intraoperative resection.[3,10] For example, leveraging β-lactamase's ability to hydrolyze amide bonds in antibiotics, fluorescent probes can be designed for drug-resistant bacteria detection and infection treatment.[11–13]

In recent years, proximity labeling techniques have flourished. These methods install catalysts on biomolecules of interest, generating highly reactive intermediates that covalently react with neighboring biomacromolecules, enabling the labeling and reporting of interacting molecules within the microenvironment.[14,15] Inspired by proximity labeling, we envisioned that hydrolases localized to specific biological regions (via genetic engineering or targeted molecular guidance) can cyclically hydrolyze spatially proximal substrates in a "localized" manner.[16,17] Consequently, installing enzyme-substrate-caged signal molecules on biomolecules of interest would enable proximity-triggered signal switching (OFF → ON) through localized hydrolysis, thereby reporting the abundance of target biomolecules in specific spatial domains. We termed this mechanism localized hydrolysis-based proximity reporting (LHPR, Scheme 1a). Its core concept lies in spatially propagating proximity information through cyclic hydrolysis to activate signals, distinguishing it from proximity labeling.

Key enzyme requirements for LHPR include: 1) Absence in mammals to prevent false-positive signals and minimize interference with native biological systems; 2) The enzyme activity can be precisely modulated to prevent false positive signal generation at the probe binding stage. We selected New Delhi metallo-β-lactamase 1 (NDM-1) to construct the reporting system. This Zn^{2+}-dependent hydrolase exists exclusively in prokaryotes, with activity regulated by Zn^{2+}

[*] W. Li, Dr. Y. Li, N. Wang, H. Wang, S. Cheng, Prof. L. Ding, Prof. H. Ju
State Key Laboratory of Analytical Chemistry for Life Science, School of Chemistry and Chemical Engineering, Nanjing University, Nanjing 210023, China
E-mail: dinglin@nju.edu.cn

H. Tian, S. Jiang, Prof. X. Wang
Institute of Advanced Synthesis, School of Chemistry and Molecular Engineering, Nanjing Tech University, Nanjing 211816, China

Dr. Y. Xue
Affiliated Jinhua Hospital, Zhejiang University School of Medicine, Jinhua 321000, China

Dr. N. Feng
State Key Laboratory of Digital Medical Engineering, School of Biological Science and Medical Engineering, Southeast University, Nanjing 211189, China

R. Jia, Prof. C. Yan
State Key Laboratory of Pharmaceutical Biotechnology, School of Life Sciences, Nanjing University, Nanjing 210023, China

Prof. C. Yan, Prof. L. Ding
Chemistry and Biomedicine Innovation Center (ChemBIC), ChemBioMed Interdisciplinary Research Center, Nanjing University, Nanjing 210023, China

Additional supporting information can be found online in the Supporting Information section

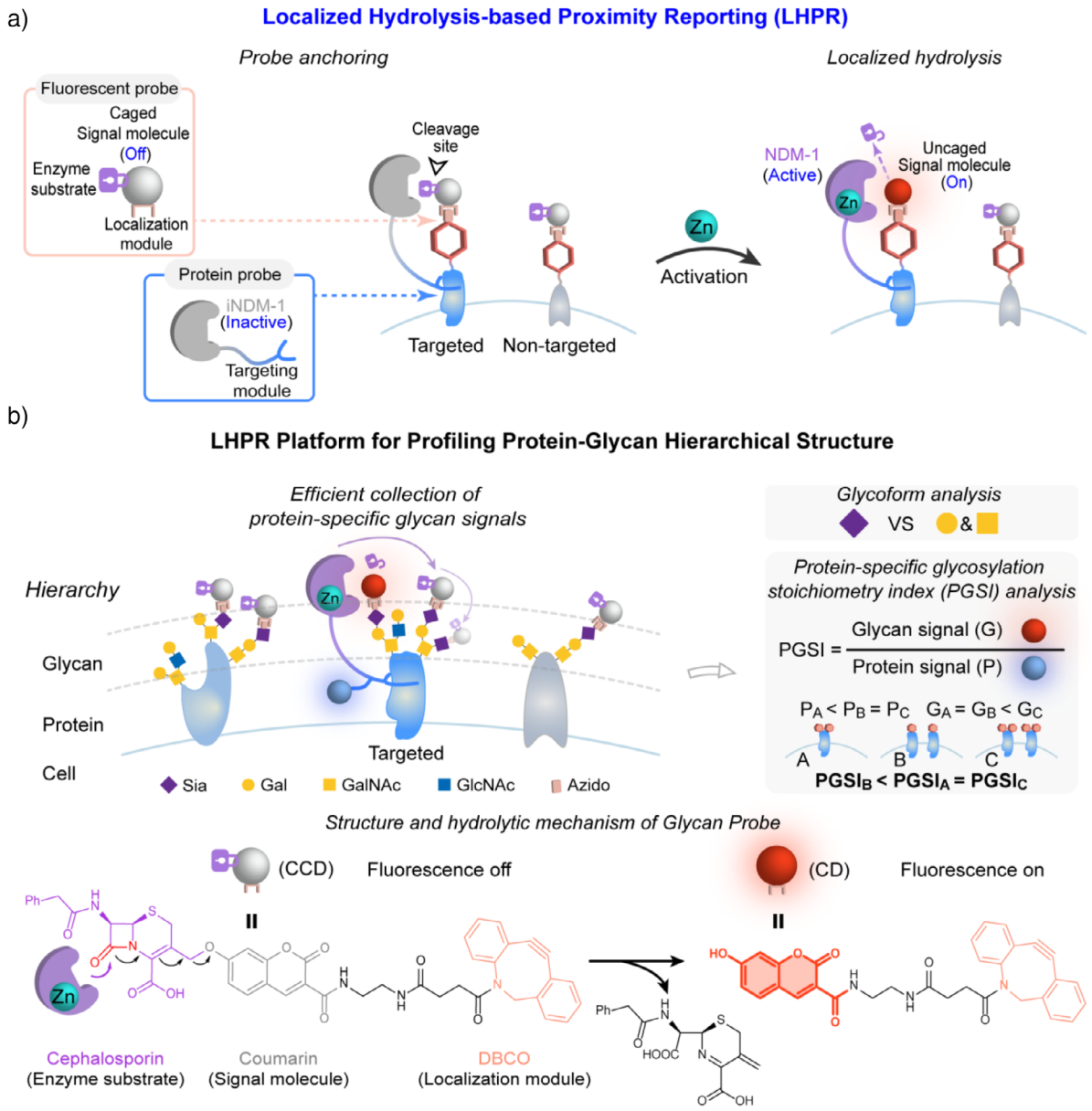

Scheme 1. Principle of localized hydrolysis-based proximity reporting (LHPR) platform and its application in protein hierarchical structure profiling.

removal/addition.[18–21] The catalytic cycling enables efficient accumulation of high-abundance proximity signals, and diverse structures at proximal sites can be detected within a unified framework by conjugating enzyme-substrate-caged signal molecules. LHPR is uniquely suited for hierarchical targets like protein glycosylation. Glycans attached to the target protein exhibit intricate compositional diversity and spatial heterogeneity,[22] critically influencing protein function and cellular phenotypes. Conventional glycomics methods struggle to establish dynamic correlations between glycan microheterogeneity and hierarchical regulation.

Herein, we developed an LHPR platform consisting of protein and glycan probes to achieve protein-specific glycan analysis. Glycans lack natural recognition molecules with high affinity and high specificity, and different labeling methods (including metabolic glycan labeling (MGL), chemoenzymatic glycan labeling (CeGL), chemical oxidation/labeling, etc.) are used for different glycans to covalently attach or generate bio-orthogonal reactive groups (e.g., azido) on the glycans.[23] Therefore, we incorporated complementary click chemistry groups (e.g., dibenzocyclooctyne, DBCO) into enzyme-substrate-caged fluorescence molecules. This enables detection of diverse glycans using a unified "protein-specific proximity-dependent activation" framework. We further proposed the principle of protein-specific glycosylation stoichiometry index (PGSI) analysis to hierarchically quantify glycosylation changes of an individual protein (Scheme 1b). Compatible with cells and tissue sections, this platform provides a powerful tool for developing disease biomarkers, drug targets, and diagnostic methods based on protein glycoforms.

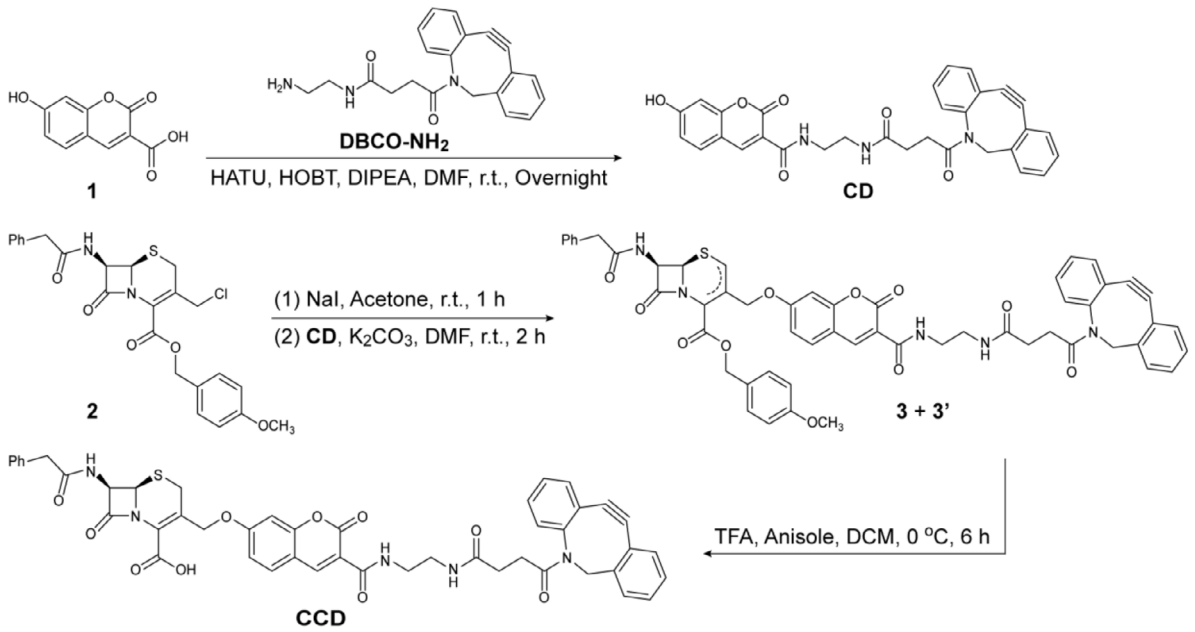

Scheme 2. Synthetic route of **CCD**.

Results and Discussion

Design and Synthesis of the Glycan Probe

The LHPR platform comprises two core components: protein probe and glycan probe. The protein probe is constructed by conjugating inactivated NDM-1 (**iNDM-1**, with Zn^{2+} removed) to a targeting module (e.g., aptamer, peptide). This module directs the probe to the target protein through specific molecular recognition. The glycan probe (**C**ephalosporin-**C**oumarin-**D**BCO, **CCD**) integrates three functional modules: i) enzyme substrate module, cephalosporin; ii) fluorescent signal module, coumarin; and iii) glycan localization module, a clickable bio-orthogonal molecule DBCO. After azido is attached to the glycans of interest by a certain glycan labeling technique, the glycan probe can be covalently linked to azido via strain-promoted azide-alkyne cycloaddition (SPAAC) reaction.[24] The fluorescence of the coumarin module is quenched due to the cephalosporin-mediated inhibition of the intramolecular charge transfer (ICT) process. Upon binding of the protein probe to the target protein, Zn^{2+} is reintroduced to reactivate NDM-1. The reactivated enzyme selectively hydrolyzes the glycan probe in close proximity by cleaving the amide bond in the molecule, which causes electron rearrangement to break the ether bond between cephalosporin and coumarin (Scheme 1b). This hydrolysis triggers the restoration of the ICT process, thereby "switching on" the coumarin fluorescence. The resulting fluorescence signal directly reports the presence and localization of the target protein-associated glycans.

CCD was synthesized by conjugating the phenolic hydroxyl group of compound **1** to cephalosporin via an ether linkage and its carboxyl group to DBCO via an amide linkage (Scheme 2 and Supporting Information 1.4). **C**oumarin-**D**BCO (**CD**) was prepared by activating compound **1**'s carboxyl group with 1-[bis(dimethylamino)methylene]-1*H*-1,2,3-triazolo[4,5-b]-pyridinium 3-oxid hexafluorophosphate (HATU) and 1-hydroxybenzotriazole (HOBT), and then coupling it to **DBCO-NH$_2$**. Iodination of compound **2** (Finkelstein reaction) afforded compound **2a**, which alkylated the phenolic hydroxyl group of the coumarin moiety in **CD**. Hydrolysis of the resulting mixture in dichloromethane/trifluoroacetic acid (DCM/TFA) yielded the final **CCD** probe.

CCD Response Behavior to NDM-1 in Solution

CCD showed a maximum absorption peak at 350 nm, which was attenuated after incubation with NDM-1 and a new absorption peak appeared at 400 nm (Figure S1). Meanwhile, the fluorescence intensity (FI) of **CCD** at 446 nm gradually increased with prolonged incubation with NDM-1, and the signal-to-background ratio (SBR) reached 13.3 at 120 min, while the FI of **CCD** without enzyme treatment was weak due to the inhibition of the intramolecular charge transfer process (Figures 1a and S2).

We determined the kinetic parameters of **CCD** as a substrate for NDM-1 using Michaelis–Menten's equation: the K_m value was 39.4 ± 2.3 μ M and k_{cat} was 0.571 ± 0.0126 s^{-1} (Figure S3). Compared with other substrates reported in the literature,[25] both the affinity and reaction rate of **CCD** for NDM-1 were slightly lower, most likely due to the increased steric hindrance by DBCO.

CCD response was concentration-dependent for NDM-1 (0-10 nM), plateauing at an SBR of 14.1 (Figure S4), and showed higher specificity for NDM-1 over other β-lactamases or BSA (Figure 1b). HPLC confirmed NDM-1-mediated conversion of soluble **CCD** (6.55 min) to **CD** (6.13 min) (Figure 1c).

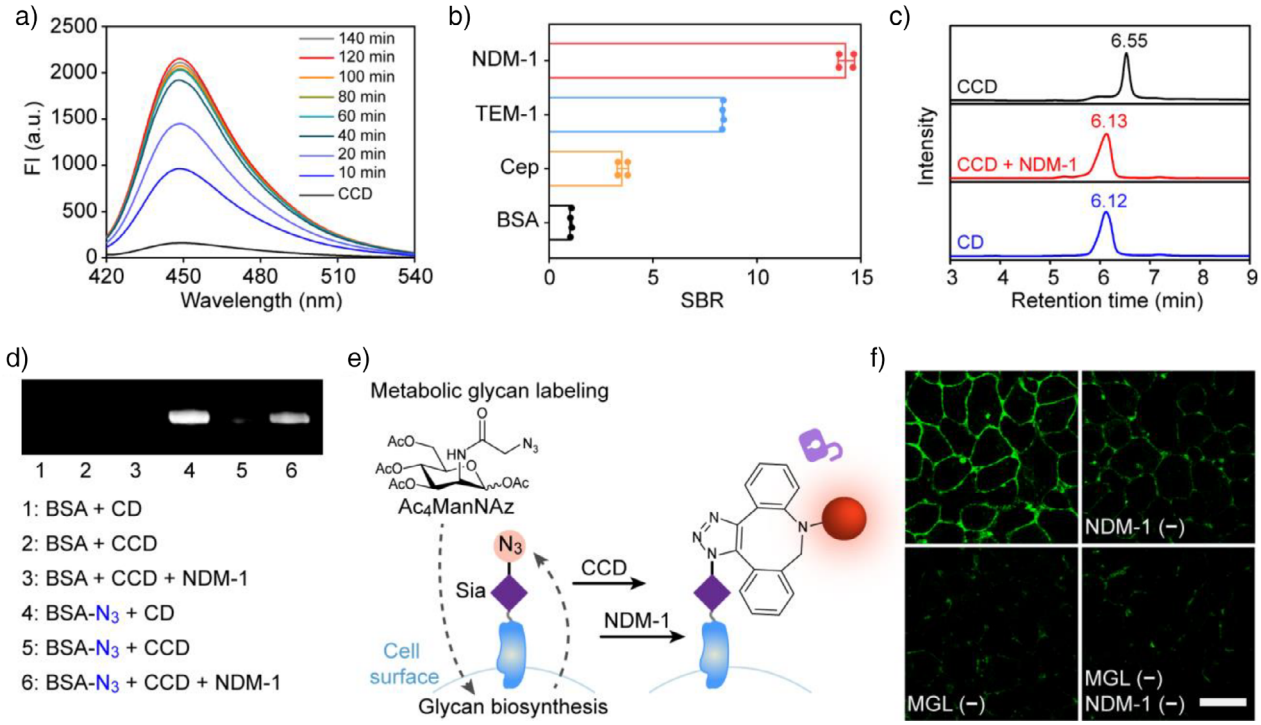

Figure 1. Response of **CCD** to NDM-1. a) Fluorescence spectra of **CCD** (5 μM) after treatment with NDM-1 (10 nM) in PBS (pH 7.4, 25 °C) for different time periods. $\lambda_{ex} = 405$ nm. b) Signal-to-background ratio (SBR) of the fluorescence intensity (FI) of **CCD** (5 μM) after 2 h incubation with NDM-1, TEM-1 β-lactamase (TEM-1), cephalosporinase (Cep), or BSA (all at 10 nM) in PBS (pH 7.4, 25 °C). c) HPLC traces of **CCD** (500 μM) before and after treatment with NDM-1 (1 μM) in PBS (pH 7.4, 25 °C) for 2 h. d) Demonstration of the anchoring and response capabilities of **CCD** on model protein BSA. In-gel fluorescence of BSA after different treatment combinations was shown. **CD**/**CCD** (0.45 mM) was incubated with BSA/**BSA-N$_3$** (15 μM) at 37 °C for 1 h; NDM-1 cleavage conditions: 500 nM, 37 °C, 30 min (see Supporting Information for full-size gel). e) Schematic illustration of the metabolic labeling of Sia and **CCD**-based visualization of cell-surface Sia. f) Demonstration of the dependence of fluorescence signal generation on cellular **CCD** installation and the presence of NDM-1 using Sia on MCF-7 cells as the model. Excitation wavelength of **CCD**: 405 nm; imaging window: 420–500 nm. Scale bar: 25 μm. The spectra in (a), and (c) and images in (d), and (f) are representative of three individual experiments, and data in (b) are presented as mean ± SD ($n = 3$).

Anchoring and Fluorescent Activation of CCD on Cell Surface Glycans

We first demonstrated the click reactivity of **CCD** using azido-modified BSA (**BSA-N$_3$**) (Figure S5).[26] **CCD** covalently anchored to **BSA-N$_3$** via SPAAC showed weak baseline fluorescence and significantly increased after NDM-1 treatment (Figures 1d and S6). In cellular studies, **CCD** (10–50 μM) exhibited negligible cytotoxicity (Figure S7). Hydrophobic insertion of a conjugate of cholesterol and **CCD** (**Cho-PEG-CCD**)[27] onto MCF-7 membranes allowed NDM-1-responsive fluorescence recovery (Figure S8). Azido-modified cells (via Cho-PEG-N$_3$) treated sequentially with **CCD** and NDM-1 showed clear membrane fluorescence, unlike controls lacking NDM-1 or azido groups (Figure S9). Using metabolic labeling[28–31] (Ac_4ManNAz) to introduce azido groups onto cell surface sialic acids (Sia) (Figures 1e and S10), optimized **CCD** anchoring achieved 37.8% labeling efficiency (Figures S11 and S12).[32] NDM-1 treatment of anchored **CCD** produced specific membrane fluorescence (Figures 1f, S13, and S14), contrasting with background signals in unlabeled or enzyme-free controls. Enzymatic reactions were performed at 4 °C to prevent probe internalization (Figure S15), with anchored **CCD** showing excellent membrane stability (<12% signal loss after 8 h incubation) (Figure S16).

Imaging of MUC1-Specific Sia on Living Cells by LHPR

Reversible regulation of NDM-1 activity is a prerequisite for achieving localized hydrolysis. We treated NDM-1 with excess ethylenediaminetetraacetic acid disodium salt (EDTA) to obtain **iNDM-1**. After incubation of **CCD** with **iNDM-1**, the fluorescence change was negligible; in contrast, treatment with **iNDM-1** + $ZnSO_4$ resulted in a rapid increase in FI and the trend of fluorescence change was similar to that of **CCD** when treated with NDM-1, except that the time to reach the plateau was slightly longer (Figure S17).

As a proof of concept, mucin 1 (MUC1), a heavily O-glycosylated protein with well-established utility as a cancer biomarker,[33,34] was chosen as the target protein, and a well-documented MUC1-specific aptamer sequence S2.2 (Apt),[35] was selected to guide **iNDM-1** for localized hydrolysis (Figure S18). Aptamers are ideal for targeting proteins as they are smaller and easier to modify than antibodies. The protein probe **iNDM-1-Apt** was synthesized by conjugating **iNDM-1** to SH-Apt via 4-(*N*-maleimidomethyl)

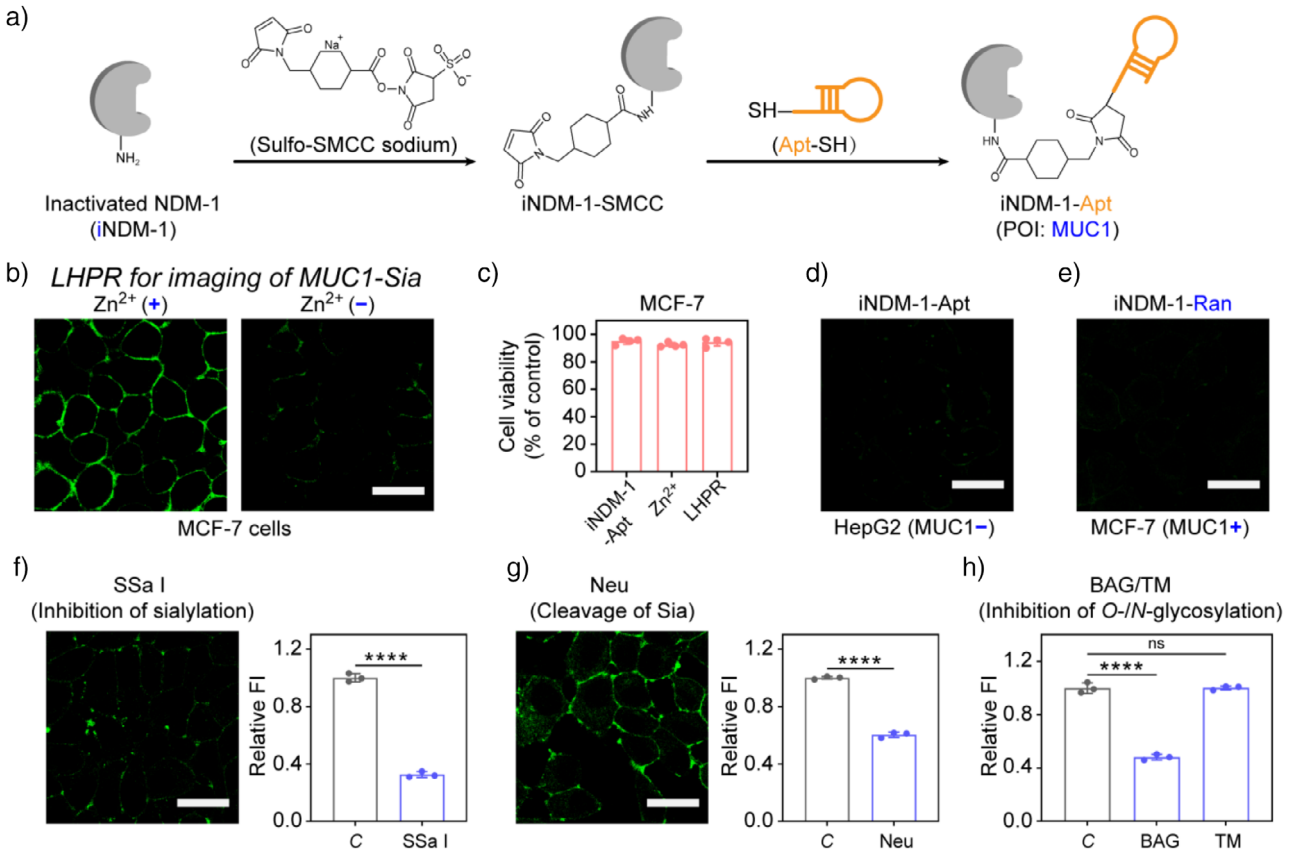

Figure 2. LHPR for imaging of MUC1-carrying Sia (MUC1-Sia). a) Schematic illustration of the synthesis of **iNDM-1-Apt**. **iNDM-1**, activity-inhibited NDM-1. b) Demonstration of the feasibility of integrating MGL and LHPR for CLSM imaging of MUC1-Sia. Cells without Zn^{2+} addition were used as a control. c) CCK-8 assay of the cytotoxicity of MCF-7 cells undergoing different treatments. d), and e) Demonstration of the protein specificity of LHPR. (d) CLSM images of HepG2 cells after LHPR operation. (e) CLSM images of MCF-7 cells after a similar LHPR operation except using **iNDM-1-Ran** instead of **iNDM-1-Apt**. Ran, random sequence. f)–h) Demonstration of the glycan specificity of LHPR by regulating cellular glycosylation with different reagents. SSa I ((f) 100 μM, *C* versus SSa I, $p < 0.0001$), BAG ((h) 2.5 mM, *C* versus BAG, $p < 0.0001$), or TM ((h) 1 μM, *C* versus TM, $p = 0.9546$) was used to treat MCF-7 cells during MGL; while for Neu (g), cells after MGL were subjected to Neu (0.5 U mL^{-1}, *C* versus Neu, $p < 0.0001$) treatment for 4 h. The cells were then subjected to **iNDM-1-Apt** based LHPR operation and CLSM imaging (see Figure S26 for images of (h)). The membrane fluorescence intensity (FI) relative to untreated samples (*C*) were obtained by counting 40 cells in three independent experiments. Excitation wavelength of **CCD**: 405 nm; imaging window: 420–500 nm. Scale bars: 25 μm. The images in (b), (d), (e), (f), and (g) are representative of three individual experiments, and data in (c), (f), (g), and (h) are presented as mean ± SD. $n = 3$ for (f), (g), (h); $n = 4$ for (c). Statistical values were calculated using an unpaired, two-tailed *t*-test. ****$p < 0.0001$, ns, not significant.

cyclohexane-1-carboxylic acid 3-sulfo-*N*-hydroxysuccinimide ester sodium salt (sulfo-SMCC) crosslinking, achieving a ~1:1 conjugation ratio (Figures 2a and S19). We confirmed that the enzymatic activity of **iNDM-1-Apt** was inhibited, and recovered to approximately 70% upon the addition of Zn^{2+} (Figure S20). This percentage was slightly lower than that of the unconjugated **iNDM-1**, presumably due to that the modification of Apt affected the enzymatic activity to some extent.

With **CCD** and **iNDM-1-Apt** successfully prepared, we selected MUC1-Sia on the surface of MCF-7 cells as a model to explore the feasibility of LHPR for analysis of protein glycosylation in situ. After the introduction of azido at the Sia site using MGL, the LHPR experimental procedure was carried out in 3 steps: 1) covalent attachment of **CCD**; 2) incubation of **iNDM-1-Apt**; and 3) activation of **iNDM-1-Apt** by addition of Zn^{2+}. Under the optimal binding conditions of **iNDM-1-Apt** (Figure S21; under these conditions, bound Apt remained stable on the cell surface for 4 h, Figure S22) and the activation conditions (Figures S23 and S24), we achieved MUC1-specific Sia imaging on the cell surface, while the fluorescence signal of Zn^{2+}-free groups was essentially negligible (Figure 2b). Finally, we performed CCK-8 experiments to confirm that the cell viability was maintained at 94.5% after performing LHPR (Figure 2c).

Demonstration of the Specificity of LHPR

Next, we chose MUC1-Sia on MCF-7 cells as the target to verify the specificity of LHPR at both protein and glycan levels. When applying the **iNDM-1-Apt** to MUC1-negative human hepatocellular carcinoma HepG2 cells, fluorescence signals were negligible (Figure 2d), confirming MUC1-dependent targeting. To further rule out nonspecific interactions, a control probe (**iNDM-1-Ran**) was constructed by conjugating

iNDM-1 to a random DNA sequence (Figure S25). No significant signal was observed in MCF-7 cells treated with **iNDM-1-Ran** (Figure 2e), underscoring the requirement for aptamer-mediated recognition in LHPR.

We investigated the glycan specificity of LHPR in two ways: 1) disrupting intracellular glycosylation and 2) remodeling glycans on the cell membrane. Soyasaponin I (SSa I) is a competitive inhibitor of the intracellular sialylation process, resulting in a decrease in α-2,3-linked Sia level on the cell surface.[36] As expected, the addition of SSa I during the MGL process resulted in a 67.4% decrease in the MUC1-Sia signal (Figure 2f). We also used neuraminidase (Neu) to cleave Sia from the outside of the cell[37] and the LHPR signal decreased by 39.7% (Figure 2g).

To further confirm the protein and glycan specificity, MCF-7 cells were treated with either benzyl-α-GalNAc (BAG) or tunicamycin (TM). BAG can inhibit the elongation of the O-glycan-initiating glycan (*N*-acetyl-D-galactosamine, GalNAc), whereas TM can inhibit *N*-glycan biosynthesis.[38] The MUC1-Sia signal decreased by 48.1% with BAG treatment but remained unchanged with TM (Figures 2h and S26), consistent with MUC1's known O-glycosylation dominance. The above results suggest the specificity of LHPR.

Docking LHPR with Different Glycan Labeling Techniques

The unique feature of using LHPR for imaging of protein glycosylation is that the glycan probe **CCD** can attach to the click motifs generated by different glycan labeling methods, either directly or indirectly via motif-converting molecules, allowing efficient collection of protein-specific glycan signals in the framework of a unified enzyme-catalyzed reaction. To illustrate this point, we docked LHPR with three other glycan labeling techniques.

The glycosyltransferase-based glycan labeling techniques introduce chemically tagged monosaccharides onto defined glycan structures, which can address the limitation of MGL in specifically targeting disaccharides.[39] We used fucosyltransferase and its monosaccharide donor substrate, guanosine diphosphate-6-azidofucose (GDP-Fuc-N_3), to introduce clickable fucose (Fuc-N_3) onto *N*-acetyllactosamine (LacNAc) of MCF-7 cell surface (Figure 3a). Subsequent **CCD** anchoring, combined with **iNDM-1-Apt** assembly and Zn^{2+}-mediated activation, achieved selective in situ imaging of MUC1-LacNAc.

Galactose oxidase (GAO) oxidizes terminal galactose (Gal) and *N*-acetylgalactosamine (GalNAc) residues on cell surfaces, converting their C6-hydroxy groups into bio-orthogonal aldehydes.[40,41] To adapt LHPR for aldehyde-bearing glycans, we developed two distinct workflows: For the first one, we coupled hydrazide-PEG_4-azido (Hz-PEG_4-N_3) to **CCD** to obtain **Hz-PEG_4-CCD**. This derivative selectively reacts with aldehyde groups, enabling LHPR-mediated imaging of MUC1-associated Gal&GalNAc (MUC1-Gal&GalNAc) on MCF-7 cells (Figure S27).

In the second workflow, aldehyde groups were first converted to azido via Hz-PEG_4-N_3, followed by **CCD** assembly. While this workflow produced a weaker signal (Figure 3b) compared to the first one, it required only 10% of the **CCD** reagent dose. These results demonstrate that LHPR's versatility can be expanded by tailoring the labeling chemistry to specific bio-orthogonal handles, broadening its applicability for glycan detection.

$NaIO_4$ can specifically oxidize the 7-OH of Sia to aldehyde groups under mild conditions.[42] Therefore, the group conversion using Hz-PEG_4-N_3 in combination with LHPR can also be used to obtain the MUC1-Sia signals on MCF-7 cells (Figure 3c). This protein-specific detection mode of Sia compensates for the unavailability of MGL in tissue sections and underlines the advantage of the flexible docking of LHPR to glycan labeling technology: expanding the applicable sample types.

In Situ Protein-Specific Detection of Terminal Glycoforms via LHPR

Terminal glycoforms, i.e., exposed monosaccharides at the ends of glycan chains attached to proteins, play pivotal roles in biological recognition, cellular adhesion, and disease mechanisms (Figure 3d).[43] Developing methods to profile these terminal glycans in situ is critical for understanding their functional and pathological significance. Sia and Gal&GalNAc (substrates for sialylation) are the most common terminal monosaccharides in mammalian glycan chains.[44,45] Hypersialylation, for instance, is strongly associated with tumor metastasis and immune evasion.[46] However, current labeling strategies for these glycans rely on distinct approaches: Sia is typically tagged via MGL or periodate oxidation, while Gal&GalNAc requires chemoenzymatic oxidation by galactose oxidase (GAO). The LHPR strategy circumvents this limitation by localizing the same hydrolysis reaction on the target protein and efficiently collecting the abundance information for dual glycans in situ.

We quantified FI for MUC1-specific Sia (Figure 2b) and Gal&GalNAc (Figure 3b) on MCF-7 cells, deriving their apparent ratio (S / G) to report terminal glycoform distribution (Figure 3e). Extending this to MUC1-positive T47D (breast cancer) and HeLa (cervical cancer) cells (Figure S28), MCF-7 exhibited higher levels of both glycans versus T47D and HeLa. While S / G ratios for breast cancer cells (MCF-7, T47D) exceeded 1, cervical cancer (HeLa) showed S / $G \approx 1$ (Figure 3e). These results highlight LHPR's capability for in situ protein-specific terminal glycoform analysis and its cellular universality.

LHPR is Versatile for Different Types of Localization Molecules

For LHPR, it is convenient to target different proteins for glycoform analysis by changing the localization molecule. We chose integrin $\alpha_v\beta_3$ on the surface of lung cancer A549 cells as a model to confirm this. Integrin $\alpha_v\beta_3$ plays an important role in angiogenesis and tumor metastasis, and the glycosylation-mediated downstream biological effects are closely associated to the development of a malignant tumor phenotype.[47] We

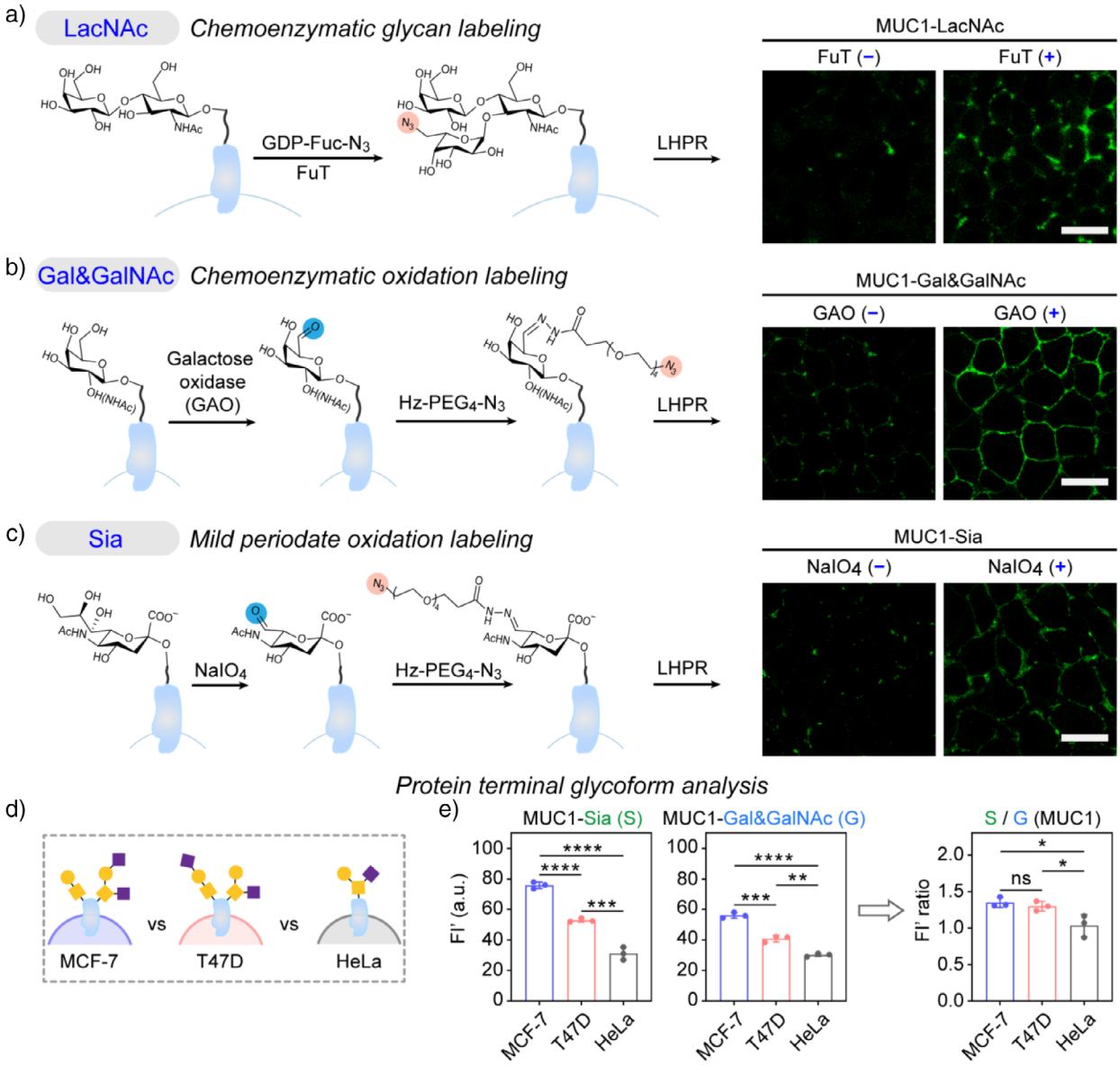

Figure 3. Protein glycoform analysis with LHPR. a)–c) Schematic of docking LHPR with different types of glycan labeling techniques and the corresponding CLSM images of MUC1-carrying glycans on MCF-7 cells after LHPR. (a) Fucosyltransferase (FuT)-based tagging for MUC1-LacNAc. (b) Galactose oxidase (GAO)-based oxidation labeling for MUC1-Gal&GalNAc. (c) Mild periodate oxidation labeling for MUC1-Sia. For (b), and (c), aldehyde groups are generated after oxidation, which can be converted to azido using hydrazide-PEG_4-azido (Hz-PEG_4-N_3). The groups without glycan labeling reagents added were used as controls. d) Schematic showing distinct terminal glycoforms on different cell types. e) Comparison of the terminal glycoforms of MUC1 on different cell types (For S, MCF-7 versus T47D, $p < 0.0001$, MCF-7 versus HeLa, $p < 0.0001$, T47D versus HeLa, $p = 0.001$; For G, MCF-7 versus T47D, $p = 0.0007$, MCF-7 versus HeLa, $p < 0.0001$, T47D versus HeLa, $p = 0.0014$; For *S* / *G*, MCF-7 versus T47D, $p = 0.4011$, MCF-7 versus HeLa, $p = 0.0298$, T47D versus HeLa, $p = 0.0495$). The ratio of FI'(Sia) to FI'(Gal&GalNAc) (i.e., *S* / *G*) was shown. FI' was calculated by subtracting the background FI (without Zn^{2+} added) from the FI (after Zn^{2+} added). FI for MCF-7 cells were from Figures 2b and 3b; FI for T47D and HeLa cells were from Figure S28. Excitation wavelength of **CCD**: 405 nm; imaging window: 420–500 nm. Scale bars: 25 μm. The images in (a–c) are representative of three individual experiments, and data in (e) are presented as mean ± SD ($n = 3$). Statistical values were calculated using an unpaired, two-tailed *t*-test. ****$p < 0.0001$, ***$p < 0.001$, **$p < 0.01$, *$p < 0.05$, ns, not significant.

coupled cyclo(RGDfk)-SH (cRGD), a peptide that specifically recognizes $\alpha_v\beta_3$, to **iNDM-1** to generate the protein probe **iNDM-1-cRGD** (Figures 4a and S29).[48,49] Both Sia and Gal&GalNAc of $\alpha_v\beta_3$ on A549 cells were probed by combining LHPR with MGL and GAO oxidation techniques (Figure 4b). $\alpha_v\beta_3$ on A549 cells had a slightly lower apparent Gal&GalNAc level compared to Sia, with an *S* / *G* ratio of 1.28. Specificity was confirmed by replacing cRGD with a control peptide (generating protein probe **iNDM-1-pep**) or pre-blocking with $\alpha_v\beta_3$ antibody—both yielding only background fluorescence (Figures 4c,d and S30). These data demonstrate the versatility of the LHPR platform for different types of localization molecules as well as different cell surface glycoproteins.

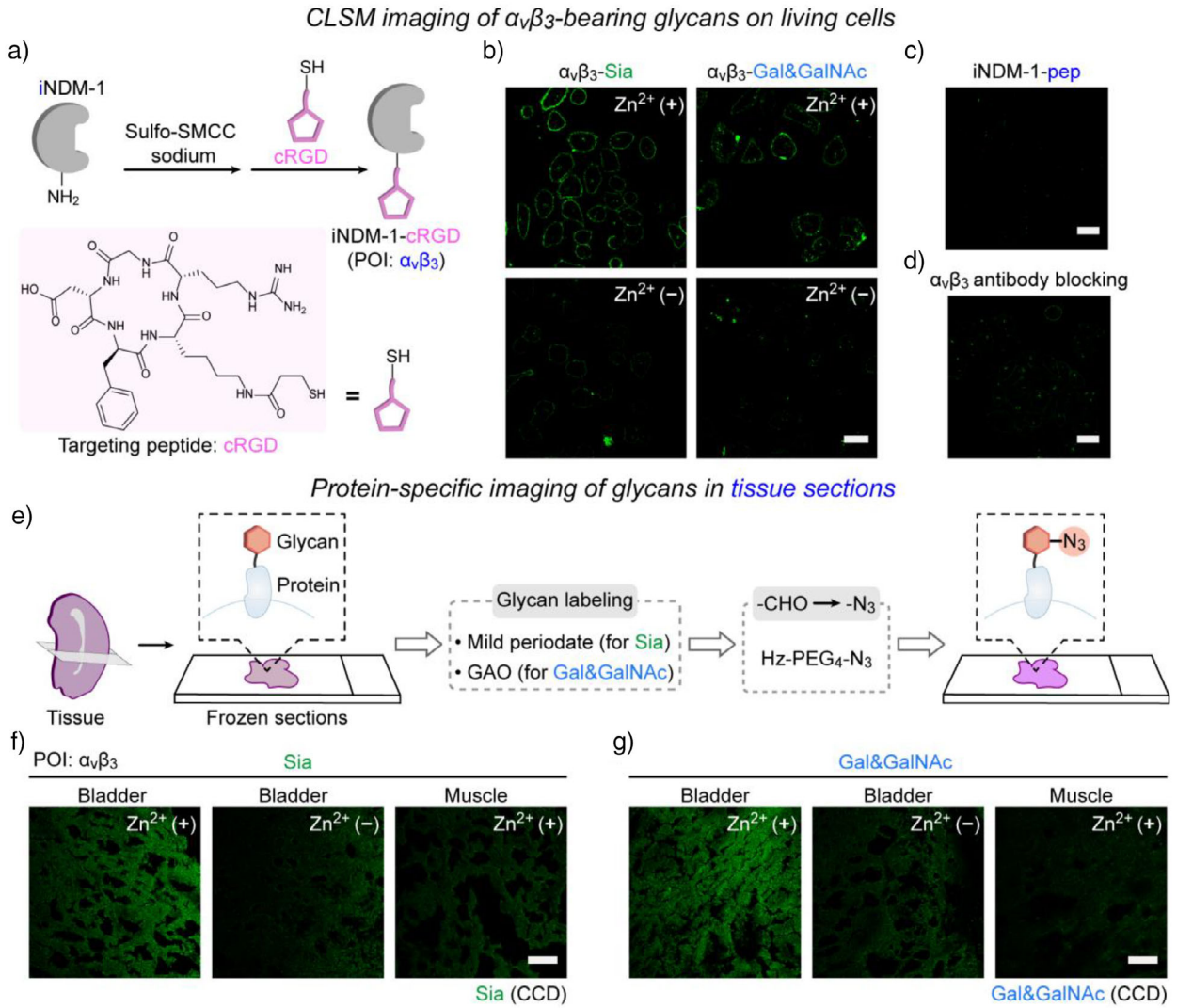

Figure 4. Peptide-guided LHPR for protein-specific glycan imaging on cellular and tissue samples. a) Schematic illustration of the synthesis of **iNDM-1-cRGD**. cRGD, cyclo(RGDfk)-SH. b) Demonstration of the feasibility of using **iNDM-1-cRGD** based LHPR to dock to MGL or GAO oxidation (+Hz-PEG_4-N_3) for CLSM imaging of $\alpha_v\beta_3$-carrying Sia and Gal&GalNAc on A549 cell surfaces. Cells without Zn^{2+} addition were used as controls. Scale bar: 25 μm. c), and d) Demonstration of the specificity of **iNDM-1-cRGD** based LHPR. (c) CLSM images of $\alpha_v\beta_3$-Sia on A549 cells after a similar LHPR operation except using **iNDM-1-pep** instead of **iNDM-1-cRGD**. Pep, a control peptide sequence. Scale bar: 25 μm. (d) CLSM images of $\alpha_v\beta_3$-Sia on A549 cells after a similar LHPR operation with an added $\alpha_v\beta_3$ antibody blocking step between **CCD** attachment and protein probe incubation operations. Scale bar: 25 μm. e) Schematic of experimental procedures for glycan labeling and functional group conversion in frozen sections. f), and g) CLSM imaging of $\alpha_v\beta_3$-Sia (f) and $\alpha_v\beta_3$-Gal&GalNAc (g) in mice bladder and muscle tissue sections. Sections without Zn^{2+} addition were used as controls. Representative images of **CCD** channels were shown. PI channels and merged images of **CCD** and PI were shown in Figures S34 and S35. Scale bars: 75 μm. Excitation wavelength of **CCD**: 405 nm; imaging window: 420–500 nm. The images in (b), (c), and (d) are representative of three individual experiments. $n = 3$ for the images in (f), and (g).

Protein-Specific Imaging of Glycans in Tissue Sections

Tissue sections, key clinical specimens preserving in situ glycan information, remain underexplored for glycosylation analysis due to the lack of tools revealing protein-specific glycoform differences. As sections cannot undergo metabolic labeling, we oxidized sialic acid (Sia) with $NaIO_4$ and galactose/galactosamine (Gal&GalNAc) with galactose oxidase (GAO) to generate aldehydes in mouse bladder and muscle tissues. These were coupled to **CCD** via Hz-PEG_4-N_3 to detect integrin $\alpha_v\beta_3$ terminal glycoforms. Global analysis showed stronger Gal&GalNAc than Sia signals in both tissues, with higher Sia in bladder (Figures S31 and S32). Immunohistochemistry confirmed elevated $\alpha_v\beta_3$ in bladder (Figure S33). After oxidative labeling, group conversion, and **iNDM-1-cRGD**-based LHPR (Figure 4e), both $\alpha_v\beta_3$-Sia and $\alpha_v\beta_3$-Gal&GalNAc were significantly higher in bladder tissue. Bladder exhibited higher $\alpha_v\beta_3$-Gal&GalNAc than $\alpha_v\beta_3$-Sia, while muscle showed slightly higher $\alpha_v\beta_3$-Sia (Figures 4f,g and S34, S35), revealing tissue-specific terminal glycoform heterogeneity.

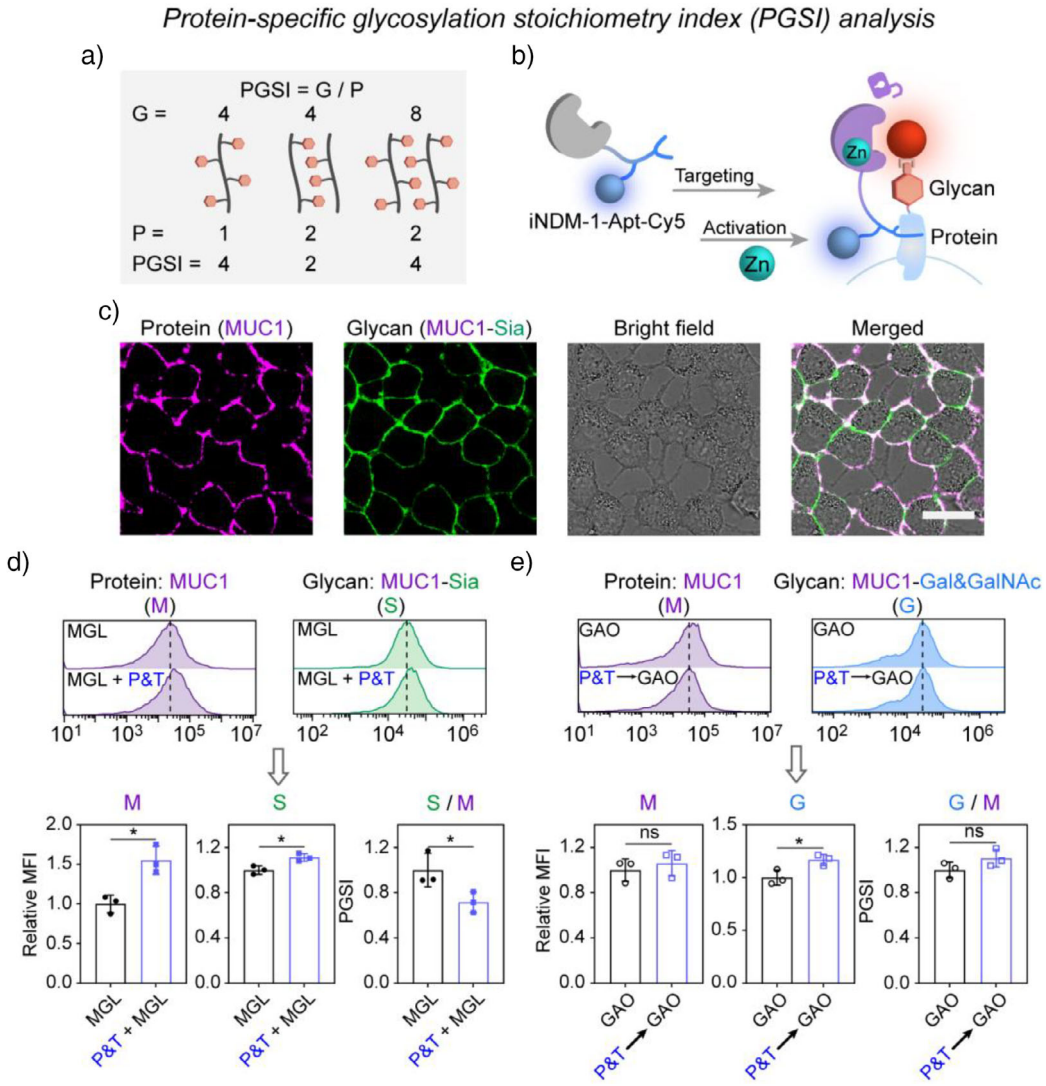

Figure 5. LHPR for protein-specific glycosylation stoichiometry index (PGSI) analysis. a) Principle of calculation of PGSI. b) Schematic showing the use of **iNDM-1-Apt-Cy5** based LHPR for simultaneous imaging of the targeted proteins and glycans. c) CLSM images of MCF-7 cells after MGL (for Sia) and **iNDM-1-Apt-Cy5** based LHPR operation. Magenta (Cy5) signal indicates MUC1, and green (**CCD**) signal indicates MUC1-Sia. Excitation wavelength of **CCD**: 405 nm; imaging window: 420–500 nm. Excitation wavelength of Cy5: 647 nm; imaging window: 660–720 nm. Scale bar: 25 μm. d) Flow cytometric analysis of MUC1 (M) and MUC1-Sia (S) on MCF-7 cells after MGL+progesterone and TNF-α (P&T) treatment (48 h) and **iNDM-1-Apt-Cy5** based LHPR operation. The relative MFI of the P&T-treated groups to untreated ones for the two hierarchies and the calculated PGSI were shown (For M, MGL versus P&T + MGL, $p = 0.0103$; For S, MGL versus P&T+MGL, $p = 0.0181$; For S / M, MGL versus P&T + MGL, $p = 0.0478$). e) Flow cytometric analysis of MUC1 (M) and MUC1-Gal&GalNAc (G) on MCF-7 cells after P&T treatment (48 h), GAO oxidation (+ Hz-PEG$_4$-N$_3$), and **iNDM-1-Apt-Cy5** based LHPR operation. The relative MFI of the P&T-treated groups to untreated ones for the two hierarchies and the calculated PGSI were shown (For M, GAO versus P&T → GAO, $p = 0.5315$; For G, GAO versus P&T → GAO, $p = 0.03$; For G / M, GAO versus P&T → GAO, $p = 0.1599$). The images in (c) and histograms in (d), and (e) are representative of three individual experiments, and data in (d), and (e) are presented as mean ± SD ($n = 3$). Statistical values were calculated using an unpaired, two-tailed *t*-test. *$p < 0.05$, ns, not significant.

Analysis of Protein-Specific Glycosylation Stoichiometry Index

The protein-specific glycan signals we detect depend on the level of protein expression and the degree of glycosylation on individual proteins. To clarify the changes in protein glycoforms, we should analyze both the protein and the glycan levels. Therefore, we propose the protein-specific glycosylation stoichiometry index (PGSI) to accurately reflect the glycosylation level of individual target proteins. This index is obtained by dividing the protein-specific glycan signal by a signal representing the protein expression level (Figure 5a). The modular design of the LHPR platform provides a simple solution for measuring the PGSI: fluorescently labeling the protein probe. Thus, upon binding, the obtained fluorescent signals on the cell surface represent the protein level. Therefore, we prepared a protein probe variant **iNDM-1-Apt-Cy5** (Figure S36) with Cy5-modified Apt, docked it to MGL, and confirmed the feasibility of imaging both proteins and protein-specific glycans simultaneously (Figure 5b,c).

It has been reported that the combined use of progesterone and tumor necrosis factor α (TNF-α) (P&T) affects the expression level of MUC1.[50] We were curious whether changes in MUC1 expression were accompanied by changes in individual glycosylation levels. Therefore, we docked the **iNDM-1-Apt-Cy5** based LHPR with MGL and GAO oxidation techniques, respectively, to examine the effects of P&T treatment on Sia and Gal&GalNAc levels on individual MUC1 (Figure 5d,e). For Sia, although MUC1-Sia was slightly increased by P&T treatment, it resulted in a 28.5% decrease in PGSI because MUC1 expression was increased by 55.2%. For the terminal Gal&GalNAc modification, P&T treatment resulted in a slight increase in PGSI, consistent with the trend for MUC1-Gal&GalNAc. These results highlight the importance of using PGSI to assess individual glycosylation changes and confirm that LHPR is a powerful tool to reveal glycoform changes in individual proteins.

Conclusion

In this work, we have constructed an LHPR platform by integrating a click-reactive, enzyme-substrate-caged fluorophore with New Delhi metallo-β-lactamase 1 (NDM-1)—a hydrolase absent in mammalian cells. This pioneering use of NDM-1 establishes a paradigm for spatiotemporally specific in situ analysis. Applied to protein glycosylation, the platform demonstrates powerful capability to resolve complex hierarchical features in biological systems. Key advantages include: 1) spatiotemporal signal accumulation via localized catalytic cycling for high-stoichiometry glycan reporting; 2) seamless docking to diverse glycan labeling techniques through click chemistry and functional group conversion; 3) modular design enabling broad compatibility with protein localization modalities and sample types.

Unlike conventional proximity labeling methods limited to amino acids and nucleic acids,[51] LHPR uniquely enables glycan-targeted proximity analysis. Furthermore, it addresses two critical limitations of existing techniques: it employs proximity-dependent activation (not labeling) without generating diffusible and extremely reactive intermediates, and leverages dual-anchored components (enzyme+substrate probe) requiring physical contact for hydrolysis, enabling superior spatial resolution and reduced background.

Using the proposed platform, we have achieved the analysis of terminal glycoforms of target proteins and individual protein glycosylation levels on living cells in situ. We propose a new parameter that reflects the elaborate nature of protein glycosylation: protein-specific glycosylation stoichiometry index (PGSI), which highlights the importance of focusing on individual protein glycosylation changes in dynamic biological processes and provides methodological support for theoretical and applied studies related to protein glycosylation. We believe that this platform has great potential to be applied to other protein modifications and extended to other biological hierarchies. The implementation of protein glycoform analysis in tissue sections can contribute to the development of new glyco-markers and glyco-intervention-based personalized treatments for diseases by combining large-scale retrospective and prospective cohort studies.

Supporting Information

The authors have cited additional references within the Supporting Information.[13,52]

Acknowledgements

The authors gratefully acknowledge support from the National Natural Science Foundation of China (22274073) and the State Key Laboratory of Analytical Chemistry for Life Science (5431ZZXM2504).

Conflict of Interests

The authors declare no conflict of interest.

Data Availability Statement

The data that support the findings of this study are available in the Supporting Information of this article.

Keywords: Fluorescence probe · Glycan · Hierarchical structure · Proximity activation · β-Lactamase

[1] S. Cecioni, R. A. Ashmus, P.-A. Gilormini, S. Zhu, X. Chen, X. Shan, C. Gros, M. C. Deen, Y. Wang, R. Britton, D. J. Vocadlo, *Nat. Chem. Biol.* **2022**, *18*, 332–341.
[2] X. Wu, R. Wang, N. Kwon, H. Ma, J. Yoon, *Chem. Soc. Rev.* **2022**, *51*, 450–463.
[3] Q. Yu, L. Zhang, M. Jiang, L. Xiao, Y. Xiang, R. Wang, Z. Liu, R. Zhou, M. Yang, C. Li, M. Liu, X. Zhou, S. Chen, *Angew. Chem. Int. Ed.* **2023**, *62*, e202313137.
[4] Z. Cheng, E. J. Thompson, L. Mendive-Tapia, J. I. Scott, S. Benson, T. Kitamura, A. Senan-Salinas, Y. Samarakoon, E. W. Roberts, M. A. Arias, J. Pardo, E. M. Galvez, M. Vendrell, *Angew. Chem. Int. Ed.* **2023**, *62*, e202216142.
[5] L. K. B. Tam, J. C. H. Chu, L. He, C. Yang, K.-C. Han, P. C. K. Cheung, D. K. P. Ng, P.-C. Lo, *J. Am. Chem. Soc.* **2023**, *145*, 7361–7375.
[6] Y. Kuriki, M. Sogawa, T. Komatsu, M. Kawatani, H. Fujioka, K. Fujita, T. Ueno, K. Hanaoka, R. Kojima, R. Hino, H. Ueo, H. Ueo, M. Kamiya, Y. Urano, *J. Am. Chem. Soc.* **2024**, *146*, 521–531.
[7] X. Wang, S. S. Liew, J. Huang, Y. Hu, X. Wei, K. Pu, *J. Am. Chem. Soc.* **2024**, *146*, 22689–22698.
[8] M. Minoshima, T. Umeno, K. Kadooka, M. Roux, N. Yamada, K. Kikuchi, *Angew. Chem. Int. Ed.* **2023**, *62*, e202301704.
[9] C.-W. Ma, K. K.-H. Ng, B. H.-C. Yam, P.-L. Ho, R. Y.-T. Kao, D. Yang, *J. Am. Chem. Soc.* **2021**, *143*, 6886–6894.
[10] W. Luo, Q. Diao, L. Lv, T. Li, P. Ma, D. Song, *Spectrochim. Acta. A Mol. Biomol. Spectrosc.* **2024**, *317*, 124411.
[11] T. Dai, J. Xie, Q. Zhu, M. Kamariza, K. Jiang, C. R. Bertozzi, J. Rao, *J. Am. Chem. Soc.* **2020**, *142*, 15259–15264.
[12] Y. Ding, Z. Li, C. Xu, W. Qin, Q. Wu, X. Wang, X. Cheng, L. Li, W. Huang, *Angew. Chem. Int. Ed.* **2021**, *60*, 24–40.

[13] H. Tian, Y. Wang, Y. Dai, A. Mao, W. Zhou, X. Cao, H. Deng, H. Lu, L. Ding, H. Shen, X. Wang, *Antimicrob. Agents Chemother.* **2022**, *66*, e00352-22.
[14] M.-G. Kang, H.-W. Rhee, *Acc. Chem. Res.* **2022**, *55*, 1411–1422.
[15] Z. Lin, K. Schaefer, I. Lui, Z. Yao, A. Fossati, D. L. Swaney, A. Palar, A. Sali, J. A. Wells, *Science* **2024**, *385*, eadl5763.
[16] S. Li, A. Mao, F. Huo, X. Wang, Y. Guo, L. Liu, C. Yan, L. Ding, H. Ju, *Mater. Today* **2021**, *49*, 85–96.
[17] X. Yu, H. Shi, Y. Li, Y. Guo, P. Zhang, G. Wang, L. Li, X. Chen, L. Ding, H. Ju, *ACS Appl. Mater. Interfaces* **2020**, *12*, 54387–54398.
[18] D. Yong, M. A. Toleman, C. G. Giske, H. S. Cho, K. Sundman, K. Lee, T. R. Walsh, *Antimicrob. Agents Chemother.* **2009**, *53*, 5046–5054.
[19] R. Wang, T.-P. Lai, P. Gao, H. Zhang, P.-L. Ho, P. C.-Y. Woo, G. Ma, R. Y.-T. Kao, H. Li, H. Sun, *Nat. Commun.* **2018**, *9*, 439.
[20] Y. Guo, J. Wang, G. Niu, W. Shui, Y. Sun, H. Zhou, Y. Zhang, C. Yang, Z. Lou, Z. Rao, *Protein Cell* **2011**, *2*, 384–394.
[21] T. Li, Q. Wang, F. Chen, X. Li, S. Luo, H. Fang, D. Wang, Z. Li, X. Hou, H. Wang, *PLoS One* **2013**, *8*, e61914.
[22] K. T. Schjoldager, Y. Narimatsu, H. J. Joshi, H. Clausen, *Nat. Rev. Mol. Cell Biol.* **2020**, *21*, 729–749.
[23] K. K. Palaniappan, C. R. Bertozzi, *Chem. Rev.* **2016**, *116*, 14277–14306.
[24] N. J. Agard, J. A. Prescher, C. R. Bertozzi, *J. Am. Chem. Soc.* **2004**, *126*, 15046–15047.
[25] H. Shi, Y. Cheng, K. H. Lee, R. F. Luo, N. Banaei, J. Rao, *Angew. Chem. Int. Ed.* **2014**, *53*, 8113–8116.
[26] W. Li, J. Zou, S. Zhu, X. Mao, H. Tian, X. Wang, *Chem. - Eur. J.* **2019**, *25*, 10328–10332.
[27] L. Poocza, F. Cipriani, M. Alonso, J. C. Rodríguez-Cabello, *ACS Omega* **2019**, *4*, 10818–10827.
[28] E. Saxon, C. R. Bertozzi, *Science* **2000**, *287*, 2007–2010.
[29] H. C. Hang, C. Yu, D. L. Kato, C. R. Bertozzi, *Proc. Natl. Acad. Sci. U.S.A.* **2003**, *100*, 14846–14851.
[30] D. Rabuka, S. C. Hubbard, S. T. Laughlin, S. P. Argade, C. R. Bertozzi, *J. Am. Chem. Soc.* **2006**, *128*, 12078–12079.
[31] M. Sawa, T.-L. Hsu, T. Itoh, M. Sugiyama, S. R. Hanson, P. K. Vogt, C.-H. Wong, *Proc. Natl. Acad. Sci. U.S.A.* **2006**, *103*, 12371–12376.
[32] Y. Zhong, L. Xu, C. Yang, L. Xu, G. Wang, Y. Guo, S. Cheng, X. Tian, C. Wang, R. Xie, X. Wang, L. Ding, H. Ju, *Nat. Commun.* **2023**, *14*, 7285.
[33] W. Chen, Z. Zhang, S. Zhang, P. Zhu, J. K.-S. Ko, K. K.-L. Yung, *Int. J. Mol. Sci.* **2021**, *22*, 6567.
[34] S. Nath, P. Mukherjee, *Trends Mol. Med.* **2014**, *20*, 332–342.
[35] C. S. M. Ferreira, C. S. Matthews, S. Missailidis, *Tumor Biol* **2006**, *27*, 289–301.
[36] C.-Y. Wu, C.-C. Hsu, S.-T. Chen, Y.-C. Tsai, *Biochem. Biophys. Res. Commun.* **2001**, *284*, 466–469.
[37] Y. Li, X. Chen, *Appl. Microbiol. Biotechnol.* **2012**, *94*, 887–905.
[38] K. Almahayni, M. Spiekermann, A. Fiore, G. Yu, K. Pedram, L. Möckl, *Matrix Biology Plus* **2022**, *16*, 100108.
[39] T. Zheng, H. Jiang, M. Gros, D. S. d. Amo, S. Sundaram, G. Lauvau, F. Marlow, Y. Liu, P. Stanley, P. Wu, *Angew. Chem. Int. Ed*. **2011**, *123*, 4199–4204.
[40] J. B. Rannes, A. Ioannou, S. C. Willies, G. Grogan, C. Behrens, S. L. Flitsch, N. J. Turner, *J. Am. Chem. Soc.* **2011**, *133*, 8436–8439.
[41] T. N. C. Ramya, E. Weerapana, B. F. Cravatt, J. C. Paulson, *Glycobiology* **2013**, *23*, 211–221.
[42] Y. Zeng, T. N. C. Ramya, A. Dirksen, P. E. Dawson, J. C. Paulson, *Nat. Methods* **2009**, *6*, 207–209.
[43] S. S. Shivatare, V. S. Shivatare, C.-H. Wong, *Chem. Rev.* **2022**, *122*, 15603–15671.
[44] J. Huang, M. Li, B. Mei, J. Li, Y. Zhu, Q. Guo, J. Huang, G. Zhang, *J. Transl. Med.* **2022**, *20*, 496.
[45] T. Bertok, E. Jane, M. Hires, J. Tkac, *Cancers* **2024**, *16*, 3786.
[46] W. Zhu, Y. Zhou, L. Guo, S. Feng, *Cell Death Discov* **2024**, *10*, 415.
[47] G. Marsico, L. Russo, F. Quondamatteo, A. Pandit, *Trends Cancer* **2018**, *4*, 537–552.
[48] M. Pfaff, K. Tangemann, B. Müller, M. Gurrath, G. Müller, H. Kessler, R. Timpl, J. Engel, *J. Biol. Chem.* **1994**, *269*, 20233–20238.
[49] Y. Li, F. Huo, L. Chen, H. Wang, J. Wu, P. Zhang, N. Feng, W. Li, L. Wang, Y. Wang, X. Wang, X. Yang, Z. Lu, Y. Mao, C. Yan, L. Ding, H. Ju, *Angew. Chem. Int. Ed.* **2023**, *62*, e202218148.
[50] N. Dharmaraj, P. Wang, D. D. Carson, *Mol. Endocrinol.* **2010**, *24*, 2253–2266.
[51] Y. Zhou, G. Wang, P. Wang, Z. Li, T. Yue, J. Wang, P. Zou, *Angew. Chem. Int. Ed.* **2019**, *131*, 11889–11893.
[52] R. C. Chadwick, S. V. Gyzen, S. Liogier, A. Adronov, *Synthesis* **2014**, *46*, 669–677.

Manuscript received: April 29, 2025
Revised manuscript received: August 05, 2025
Accepted manuscript online: August 06, 2025
Version of record online: ■■, ■■